Modeling of Dynamic Recrystallization Kinetics in Ce containing Mg alloys

Storey, G.K.[1]; Eres-Castellanos, A.[1,*]; Sutton, S.[2]; McBride, B.N.L[1], Peterson, N.[1]; Hartman, D.[2]; Clarke, A.J.[1]; Clarke, K.D.[1]

[1]Center for Advanced Non-Ferrous Structural Alloys (CANFSA), Metallurgical and Materials Engineering Department, Colorado School of Mines, Golden, CO 80401, canfsa.org (United States of America)

[2]Mag Specialties Inc., Denver, CO, 80210 (United States of America)

*correspondence: erescastellanos@mines.edu

Abstract

ZK60 alloys are known to have high mechanical strength relative to other Mg alloys. Composition variations in precipitate and solute content of ZK60 Mg alloys, with Zn variations and Ce substitutions, allows for the formation of higher melting point precipitates, impact dynamic recrystallization (DRX) behavior, microstructure, and mechanical properties. Creating constitutive models of the DRX process in various Mg alloys can help guide processing to efficiently create products with desirable microstructures. In this work, hot compression testing at various strain rates and temperatures was carried out. It has been shown that greater peak true stresses are required for DRX in alloys processed at lower temperatures and higher strain rates. Moreover, increases in Zn and Ce content increase the stress that the microstructure can absorb before DRX starts. Finally, Electron Backscattered Diffraction mapping shows how texture is decreased by DRX, as compared to the as-received conditions, and how DRX was more advanced for low Zr, low strain rate conditions, consistently with the developed model. Based on these experimental results, a constitutive model to quantify the relationship between the Zener-Hollomon parameter and peak stress was developed. The model showed to reflect the experimentally obtained results accurately.

1. Introduction

ZK60 alloys are known to have high mechanical strength relative to other Mg alloys [1]. Low melting point precipitates, such as Mg_2Zn, can cause incipient melting during thermomechanical processing if temperatures are too high [2]. The substitution of rare earth elements, such as Ce, for Zn allows for the formation of higher melting point precipitates [3], improving elevated temperature properties and higher temperature processing windows [4]. Ce additions are also known to enhance corrosion resistance, improve creep resistance, and ultimately accelerate dynamic recrystallization (DRX) [5]. Conventional Mg alloys exhibit improved formability at higher temperatures when non-basal slip systems are activated, further facilitating dislocation slip [6,7]. In metal deformation processing, DRX is an important process which significantly impacts the resultant microstructure and mechanical properties, through grain refinement and texture weakening. [2,8] There is limited knowledge about the formation of preferred crystallographic orientations in Mg alloys due to the possible deformation mechanisms, such as continuous DRX (CDRX), discontinuous DRX (DDRX) and twin DRX [9]. The CDRX mechanism is known to occur via cross-slip during compressive deformation [10], DDRX occurs by prior grain boundary protrusion toward surrounding, high dislocation density grains, while twin DRX occurs at twin intersections or fragments. In alloys with rare earth elements, particlestimulated nucleation (PSN) in the vicinity of second phase particles has also been shown to occur [11]. Texture weakening in Mg alloys has been associated with PSN, as well as other phenomena including particle pinning, solute drag, and heterogeneous deformation promoting shear band formation [11]. Fu et al. [12] studied DRX mechanisms in Mg-Zn-Mn alloys micro-alloyed with Sm, La, and/or Ca and determined that DDRX and PSN mechanisms weakened the basal texture. The occurrence of CDRX was observed by Xu et al. [13] in a Mg-13Gd-4Y-2Zn-0.5Zr (wt%) alloy during compression-torsion deformation at 450°C.

Creating constitutive models for DRX as a function of processing parameters (e.g. ε, $\dot{\varepsilon}$, T) in various Mg alloys can help guide efforts to design thermo-mechanical processing routes to create desired microstructures. For Mg alloys, flow stresses increase with strain due to work hardening until they reach a peak stress, σ_{p}, as DRX occurs after a critical strain is reached, ε_c [14]. In this work, the peak stress, determined from measured flow curves, was correlated to the deformation strain rate and temperature through the use of the Zener-Hollomon parameter (Z), which has been used in previous studies of DRX kinetics in other alloy systems, including Mg alloys. [15–19] Given the current interest in Mg alloys with rare earth elements, it is especially interesting to define constitutive models showing the relationship between the peak stress and Z for these alloys. Five different modified ZK60 compositions, containing different levels of Zn and Ce were subjected to high temperature deformation at different temperatures and strain rates. The effect of temperature and strain rate on flow stress behavior and texture was also evaluated.

2. Experimental

The alloys used for this study are modified ZK60 (Mg-Zn-Zr) compositions, with deliberate variations in Zn levels and a replacement of Ce for Zr in various amounts. ZK60 is an extrusion alloy that experiences precipitation hardening and exhibits finer microstructures after solidification, hot working, or annealing processes. The composition matrix is separated into three levels of Zn, varying the hypothesized solute content, and three levels of Ce, varying the hypothesized precipitate volume, as can be observed in Table *1*. The variations in Zn and Ce within these alloys theoretically result in changes to second phase insoluble particle type, volume fraction, and distribution. The pinning levels, calculated by Pandat's CompuTherm using the 2023 Mg database and included in the mentioned table, were provided by Mag Specialties Inc. ZK60 is ideally suited for this study, because it is a commercial alloy with insoluble Mg-Zr precipitates that influence DRX kinetics and texture. The samples for this study were machined into small cylindrical compression specimens with a diameter of 10 mm and a height of 15 mm, with the cylinder height along the extrusion direction.

Table 1. Composition matrix for five alloys studied, varied by pinning phases and solute level

	Complete Solid Solution	**~ 1% pinning phases**	**~ 3% pinning phases**
Low solute	-	**Alloy LZ-0.4Ce** Mg-1.40Zn-0.38Ce	-
Med solute	-	**Alloy MZ-0.4Ce** Mg-3.52Zn-0.38Ce	-
High solute	**Alloy HZ-0Ce** Mg-4.21Zn	**Alloy HZ-0.1Ce** Mg-5.26Zn-0.12Ce	**Alloy HZ-0.3Ce** Mg-6.78Zn-0.31Ce

Electron backscatter diffraction (EBSD) was completed on all alloys and processing conditions. After compression testing, each sample was mounted, ground, and polished to 0.05 µm colloidal silica and etched after each polishing step in a solution of 4.2g picric acid, 70 mL ethanol, 10 mL glacier acetic acid, and 10 mL deionized water, for 10 s [20]. The polished surface for these samples was parallel to the extrusion direction, for the as-received material, and the compression direction, for the deformation samples. Additionally, all as-received conditions were also EBSD-scanned to use as a reference. EBSD mapping analysis was performed with a 20 kV electron beam, 18 mm working distance, and 2 µm step size. Each inverse pole figure (IPF) map was processed with Neighbor Pattern Averaging & Indexing (NPAR) in the EDAX® Orientation Imaging Microscopy (OIM™) software.

Uniaxial compression tests on small cylindrical samples of each of the five alloys was conducted on a Gleeble 3500 thermal-mechanical simulator. All samples were compressed to a final true strain of 0.8 and were deformed at approximate engineering strain rates of 0.001, 0.01 and 0.1 s^{-1} at either 350 or 400 °C. One set of thermocouples was welded on the surface at half height of each sample and used to monitor temperature throughout the test. The samples were lubricated at the surface of each anvil with layers of Ni paste and flexible graphite. Each sample was heated at 5 °C/s under force control to the deformation temperature (350 or 400 °C), held in displacement control for 30 s to ensure the temperature throughout the sample was homogenous, deformed to approximately 0.8 true strain and quenched with compressed air (Figure 1). Load-displacement data was obtained from the compression tests and converted to true stress-true strain using standard conversion equations. This data gives way to analysis of flow behavior and microstructural characterization.

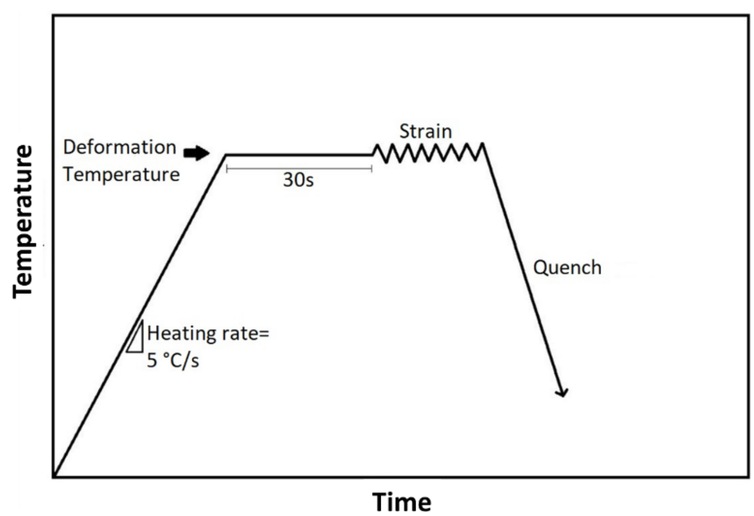

Figure 1. Gleeble testing schematic, performed at deformation temperatures of 350 °C or 400 °C and strain rates of 0.001 s^{-1}, 0.01 s^{-1} and 0.1 s^{-1}.

3. Results and discussion

3.1. Effect of DRX on flow behavior and DRX kinetics modeling

True stress-strain curves for all five alloys tested at all processing conditions are presented in Figure 2. A flow stress curve is normally separated by a work-hardening stage, transition stage, softening stage and steady stage. In general, curves in Figure 2 increase to a maximum flow stress, called peak stress (σ_p) and then decrease to a steady state. The onset of DRX is known to happen at a critical stress (σ_c), lower than σ_p, which is achieved at earlier strain stages. Curves represent how work softening is more noticeable at higher strain rates and at lower temperatures.

In this work, the relationship between the Zener-Hollomon parameter Z and the peak stress in flow stress curves σ_p was calculated for the five alloys of study. To obtain such relationship for each alloy of study, the true stress-true strain curves shown in Figure 2 are used to first calculate both σ_c and σ_P values [21]. To do so, a third order polynomial is fit to each true stress-strain curve up to the peak stress. The used polynomial function, which effectively fits data with prolonged and multiple peaks, is shown in Equation 1 [17],

$$\theta = A\sigma^3 + B\sigma^2 + C\sigma + D \quad (1)$$

where $\theta = \frac{d\sigma}{d\varepsilon}$ and constants A, B, C and D allow for calculations of certain DRX conditions. When this equation is differentiated, as shown in Equation 2 [17],

$$\frac{d\theta}{d\sigma} = 3A\sigma^2 + 2B\sigma + C \quad (2)$$

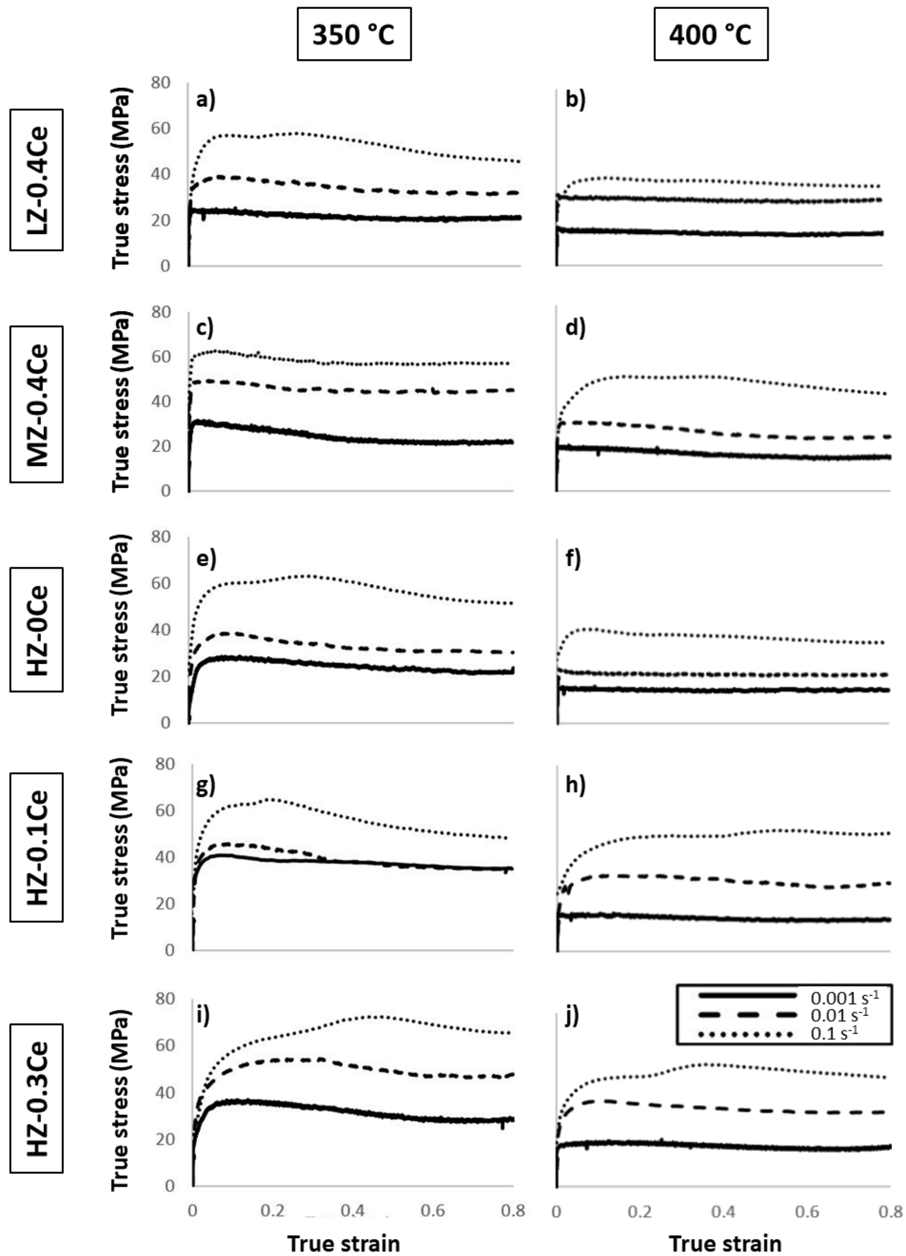

Figure 2. Flow curves of the five modified ZK60 alloys varying by both temperature and strain rate.

The peak stress can be calculated as the stress value for which the derivative is zero. The calculation of critical stress σ_c according to the derivative can be done as shown in Equation 3 [17]:

$$\frac{d^2\theta}{d\sigma^2} = 0 \rightarrow 6A\sigma_c + 2B = 0 \rightarrow \sigma_c = \frac{-B}{3A} \quad (3)$$

The fitted functions for each alloy, temperature and strain rate can be found in the Table S1 of Supplementary Material, as well as the values for σ_c and σ_P. Note that σ_c increases linearly with σ_P, which has been previously reported in the literature for steels [17], proving that both values can be effective at showing trends with respect to DRX kinetics.

Figure 3 includes the effect of alloy content, temperature and strain rate on σ_p, displaying that increases in Zn and Ce content increase the stress that the microstructure can absorb before DRX starts. With respect to the effect of temperature, it can be seen that a greater true stress is required for DRX in alloys processed at lower temperatures and higher strain rates.

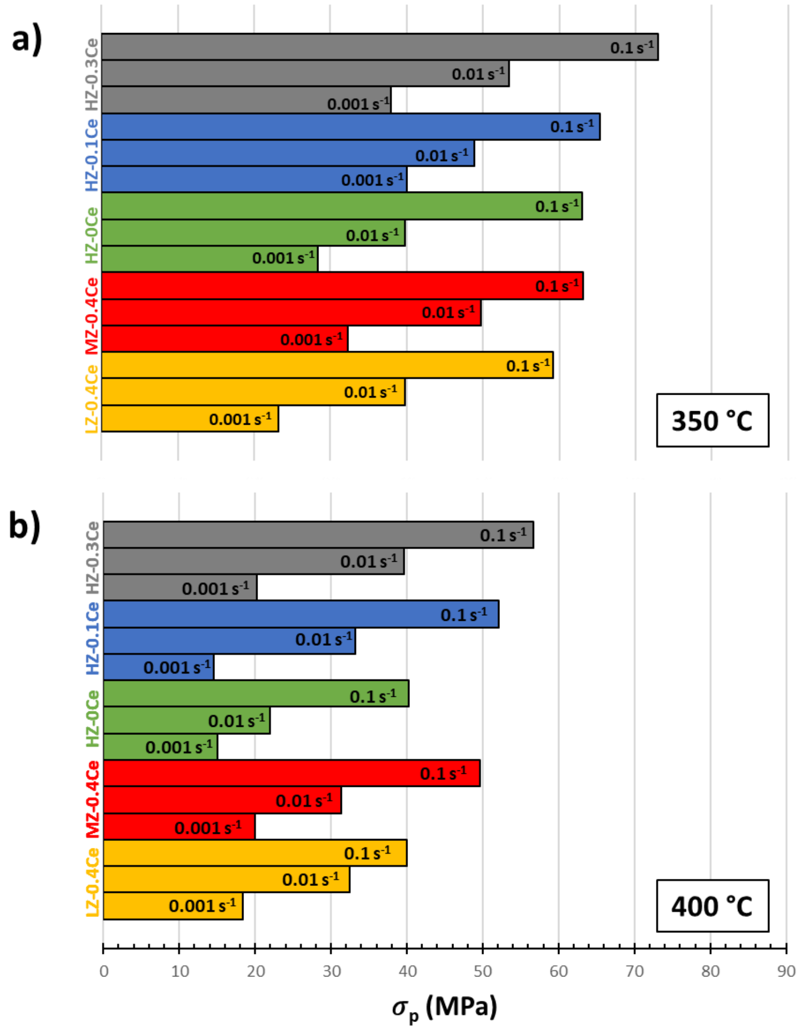

Figure 3. Influence of alloy composition and strain rate on σ_p at 350°C (a) and 400°C (b) of modified Mg-Zn-Ce alloys.

Subsequently, each θ/σ polynomial relation and associated σ_c are tabulated and utilized to determine Z and deformation activation energy (Q) by Equations 4-6 [17],

$$\dot{\varepsilon} = A_1\, \sigma^{n_1} = A_2 exp(\beta\sigma) = A(sinh(\alpha\sigma))^n exp\left(-\frac{Q}{RT}\right) \quad (4)$$

$$Z = \dot{\varepsilon}\, exp\left[\frac{Q}{RT}\right] = A(sinh(\alpha\sigma))^n \quad (5)$$

$$Q = R\left[\frac{\partial ln\varepsilon}{\partial ln(sinh(\alpha\sigma))}\right]_T \cdot \left[\frac{\partial lnsinh(\alpha\sigma)}{\partial\left(\frac{1}{T}\right)}\right]_{\dot{\varepsilon}} \quad (6)$$

where R is the gas constant (8.314 J/mol K), σ is flow stress, T is the deformation temperature and n, A_1, β, A_2, and α are material constants. The value of n_1 is obtained from the linear regression of ln $\dot{\varepsilon}$-σ_p using Equation 4 [17], while the values of β are determined by the slope of the linear regression of ln$\dot{\varepsilon}$-ln σ_p. The values of n_1, β, and α values ($\alpha = \beta/n_1$) are included in Table S2 of Supplementary Material. From these values, one can calculate the linear slopes $\left[\frac{\partial ln\varepsilon}{\partial ln(sinh(\alpha\sigma))}\right]_T$ and $\left[\frac{\partial lnsinh(\alpha\sigma)}{\partial\left(\frac{1}{T}\right)}\right]_{\dot{\varepsilon}}$, enabling to calculate Q as defined in Equation 6. The Q value for each $\dot{\varepsilon}$ and T is presented in Supplementary Material, Table S1, and shown graphically in Figure 4. The obtained values lie in the range 25-225 kJ/mol, showing a significant variability with respect to the activation energy obtained for pure Mg (135 kJ/mol) [22] and for the commercial ZK60 alloy (115-153 kJ/mol) [22–24]. Compositional changes of the alloys of study, with respect to these two references, are most likely the reason of such a Q variability. Q increases with Zn and Ce contents, denoting that DRX is impeded by the addition of these elements. Samples with higher Zn content, as well as higher Ce content, have slower DRX and require more energy for the process to begin. Moreover, greater dependence on Ce additions is observed than for Zn additions. With respect to the effect of pinning phases, it seems that, on average, a higher fraction of pinning phases (as classified in Table 1) leads to an increase of the activation energy Q.

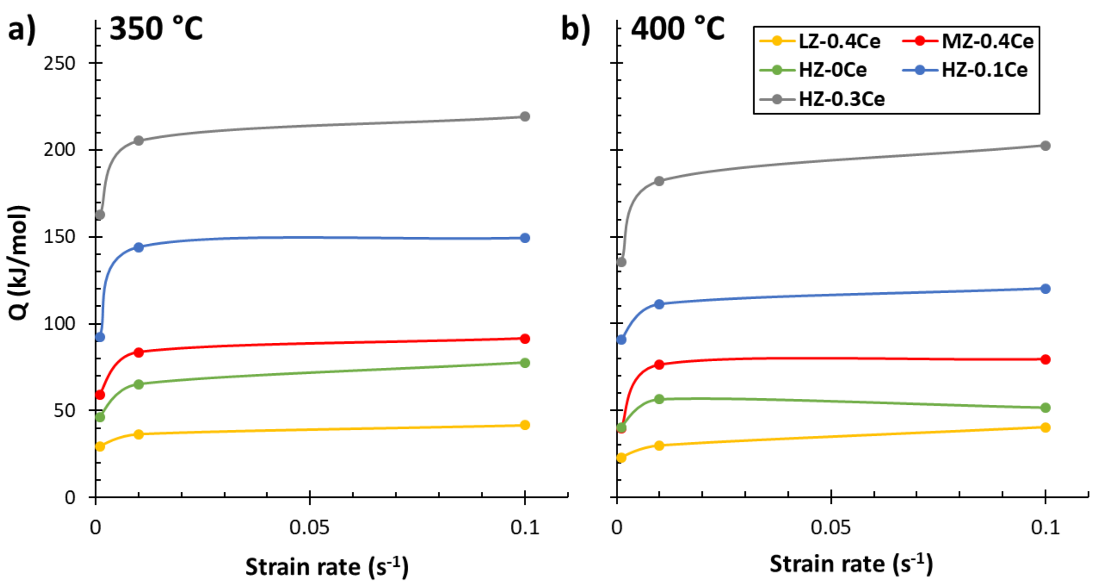

Figure 4. Calculated Q values vs. strain rate at 350°C (a) and 400°C (b).

After Q-values are known, Z values are calculated based on Equation 5. These calculated Zener-Hollomon parameter values are shown in Table S2 of Supplementary Material. Z-values describe the effect of both strain rate and temperature on flow stress and DRX. Lower Z values lead to higher DRX rates and fractions with less deformation degree [15]. Finally, Equation 7 was fitted by using the linear relationship shown in Figure 5, where the slope represents stress exponent, n, and the intercept is the constant A. The fitted parameters can be found in the Supplementary Material, in Table S2, while the fitted expressions of Z as a function of peak stress can be found in Table *2*.

$$\sigma_p = \frac{1}{\alpha}\left(\left(\frac{Z}{A}\right)^{\frac{1}{n}} + \left(\frac{Z}{A}\right)^{\frac{2}{n}} + 1\right)^{\frac{1}{2}} \tag{7}$$

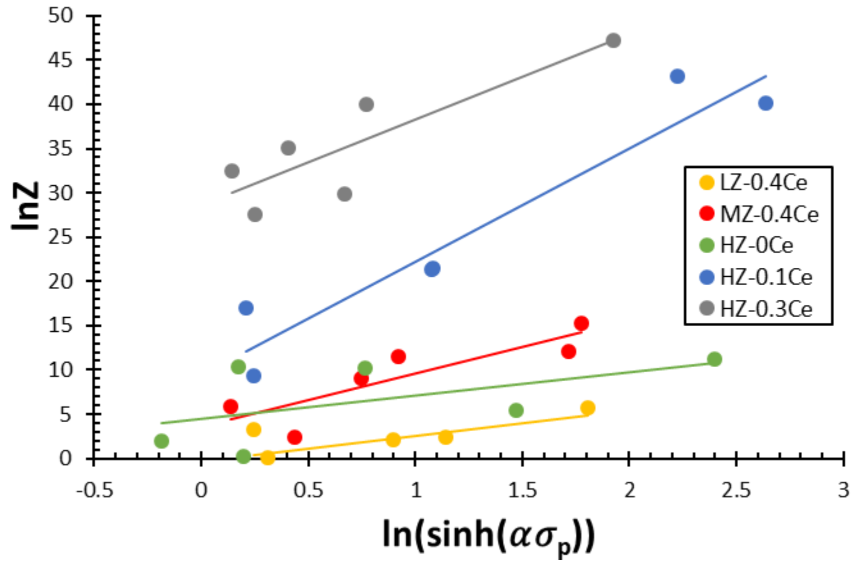

Figure 5. Relationship of flow stress and the Zener-Hollomon parameter at each processing condition. The linear regression of each alloy dataset provides the stress exponent, n, and constant A.

Table 2. Function of Zener-Hollomon parameter (Z) and flow stress (σ_p) as linear regression equation for each alloy. The slope represents stress exponent, n, and the intercept is constant A.

Alloy	lnZ-ln(sinh($\alpha\sigma_p$))
LZ-0.4Ce	lnZ = 2.8711ln(sinh($\alpha\sigma_p$)) - 0.2696
MZ-0.4Ce	lnZ = 6.0024ln(sinh($\alpha\sigma_p$)) + 3.6255
HZ-0Ce	lnZ = 9.6003ln(sinh($\alpha\sigma_p$)) + 28.687
HZ-0.1Ce	lnZ = 12.766ln(sinh($\alpha\sigma_p$)) + 9.4806
HZ-0.3Ce	lnZ = 2.6505ln(sinh($\alpha\sigma_p$)) + 4.4968

3.2. Effect of DRX on microstructure

Finally, the effect of DRX on texture was evaluated. Figure 6 and Figure 7 show the IPF maps corresponding to the as-received conditions, as well as to the post-deformation structures at 350 ºC (Figure 6) and 400 ºC (Figure 7). Coloring corresponds to the out of plane directions; perpendicular to the extrusion direction (ED) and to the compression direction (CD) –both of them defined on the top subfigures. It can be observed how the as-received samples showed a predominant basal ≈<0001> ⊥ ED fiber, in good agreement with previous works on cold extrusion texture in Mg alloys [25,26]. Post-deformation samples are fully recrystallized, based on their grain morphology and texture, regardless of the deformation temperature and strain rate. Note that Mg samples with a similar initial texture and compressed along the same direction that the one used in this work have shown a texture characterized by a ≈<0001> // CD fiber [27], in good agreement with the observed IPF colors. Moreover, results show how reduced amounts of Zr or slower strain rates cause larger post-DRX grain size. These results indicate that all microstructures were fully recrystallized after the applied deformations. Moreover, results also show that DRX was completed for shorter times and grain growth was more advanced for low Zr, low strain rate conditions. These trends are consistent with the previously obtained activation energy results, which showed that samples with higher Zn content, as well as those deformed at a higher strain rate, have slower DRX and require more energy for the process to begin. Consistently, previous works have shown that recrystallized grain size increases with decreasing Z values [27].

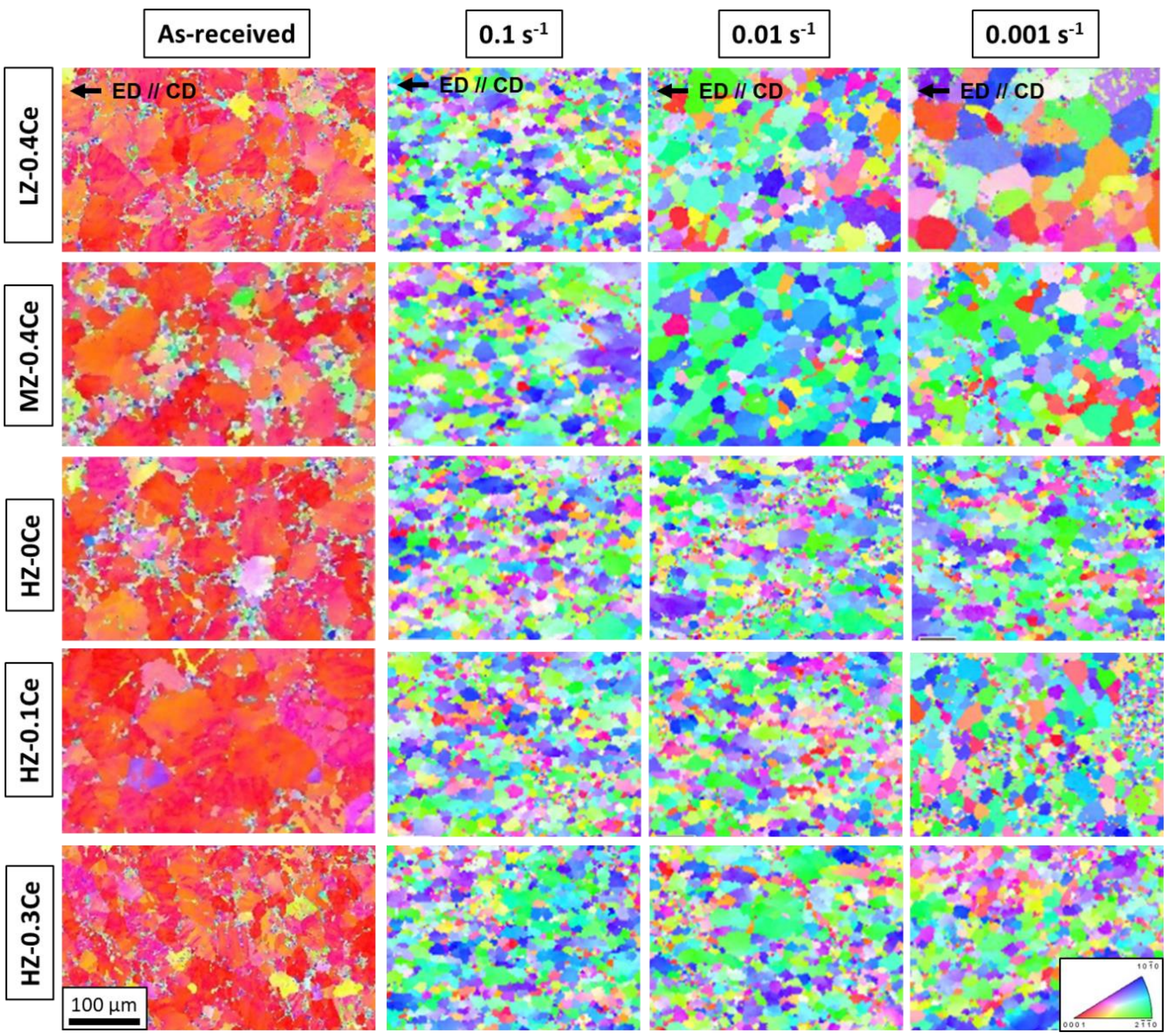

Figure 6. Representative IPF maps at strain rates 0.1 s^{-1}-0.001 s^{-1} and 350 °C for each alloy, where coloring corresponds to the direction out of plane. The extrusion direction (ED), parallel to the compression direction (CD), is represented by arrows on the top subfigures.

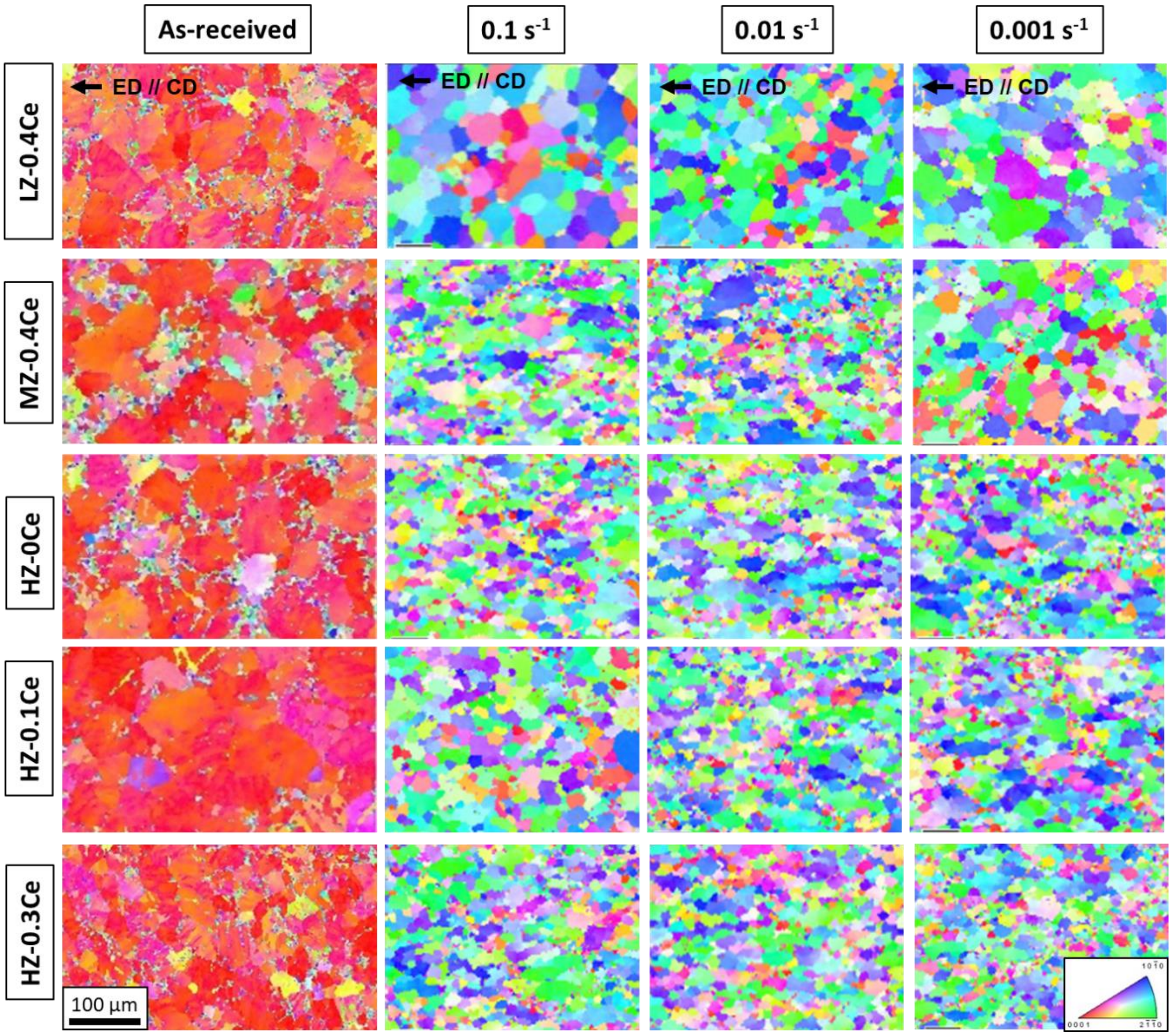

Figure 7. Representative IPF maps at strain rates 0.1 s^{-1}-0.001 s^{-1} and 400 °C for each alloy, where coloring corresponds to the direction out of plane. The extrusion direction (ED), parallel to the compression direction (CD), is represented by arrows on the top subfigures.

4. <u>Conclusions</u>

The DRX kinetics during compression testing at elevated temperatures and resultant microstructural properties in a set of designed Mg-Zn-Ce alloys were investigated in this study to give further insight into the effect of varying solute and precipitate content. The following conclusions were determined.

1. Samples with higher Zn content, as well as higher Ce content, have slower DRX and require more energy for the process to begin. This trend is directly associated to Q-values, which increase with Zn and Ce contents, denoting that DRX is impeded by the addition of these elements.
2. Greater dependence of Q on Ce additions is observed than for Zn additions. Both σ_p, determined via flow curves, and σ_c, determined through calculations, are an accurate representation of DRX initiation.

3. The determined constitutive equations for the DRX process, where Z-values are calculated as a function of peak flow stress for the alloys of study, can be used to determine industrially relevant processing parameters, given different processing conditions.
4. Lower Zr, low strain rate conditions showed a more advanced DRX state, as its kinetics were faster.

Acknowledgements

The authors acknowledge support by the Center for Advanced Non-Ferrous Structural Alloys (CANFSA), a National Science Foundation Industry/University Cooperative Research Center (I/UCRC) (Award No. 1624836) at the Colorado School of Mines. Mag Specialties, Inc. supplied and designed all alloys evaluated during the project duration.

Conflicts of interest

On behalf of all authors, the corresponding author states that there is no conflict of interest.

References

1. M. M. Avedesian and H. Baker, *ASM Specialty Handbook: Magnesium and Magnesium Alloys* (ASM international, 1999).
2. A. Hadadzadeh, S. K. Shaha, M. A. Wells, H. Jahed, and B. W. Williams, in *Magnesium Technology 2017* (Springer, 2017), pp. 513–519.
3. Z. Zhu and A. D. Pelton, Journal of Alloys and Compounds **652**, 426 (2015).
4. H. Yu, Y. M. Kim, B. S. You, H. S. Yu, and S. H. Park, Materials Science and Engineering: A **559**, 798 (2013).
5. E. Silva, R. H. Buzolin, F. Marques, F. Soldera, U. Alfaro, and H. C. Pinto, Journal of Magnesium and Alloys **9**, 995 (2021).
6. S. R. Agnew and Ö. Duygulu, International Journal of Plasticity **21**, 1161 (2005).
7. R. Verma, L. G. Hector, P. E. Krajewski, and E. M. Taleff, Jom **61**, 29 (2009).
8. T. Sakai and J. J. Jonas, Acta Metallurgica **32**, 189 (1984).
9. S. Fatemi and H. Paul, Materials Chemistry and Physics **257**, 123726 (2021).
10. A. Galiyev, R. Kaibyshev, and G. Gottstein, Acta Materialia **49**, 1199 (2001).
11. J. Dong, J. Sun, L. Jin, Z. Zhang, and W. Ding, Proceedings of 135h International Conference on Fracture 1 (2013).
12. L. Fu, Q. Le, W. Hu, J. Zhang, and J. Wang, Journal of Materials Research and Technology **9**, 6834 (2020).
13. P. Xu, J. Yu, and Z. Zhang, Materials **12**, 2773 (2019).
14. J. Liu, Z. Cui, and C. Li, Computational Materials Science **41**, 375 (2008).
15. L. Li, Y. Wang, H. Li, W. Jiang, T. Wang, C.-C. Zhang, F. Wang, and H. Garmestani, Computational Materials Science **166**, 221 (2019).
16. H. Mirzadeh, M. Roostaei, M. H. Parsa, and R. Mahmudi, Materials & Design **68**, 228 (2015).
17. A. Najafizadeh and J. J. Jonas, ISIJ International **46**, 1679 (2006).
18. N. Safara Nosar, F. Sandberg, and G. Engberg, in (Trans Tech Publ, 2018), pp. 458–467.
19. J. Duan, Y. Tan, L. Ji, W. Liu, J. Zhang, and R. Liu, Progress in Natural Science: Materials International **25**, 34 (2015).
20. T. Lin, J.-X. Zhou, C.-N. Jing, Y.-T. Liu, L.-L. Zhang, and X.-B. Meng, High Temperature Materials and Processes **39**, 200 (2020).
21. H. Mecking and U. Kocks, Acta Metallurgica **29**, 1865 (1981).
22. H. Mirzadeh, Materials Chemistry and Physics **152**, 123 (2015).
23. Y.-J. Qin, Q.-L. Pan, Y.-B. He, W.-B. Li, X.-Y. Liu, and X. Fan, Materials Science and Engineering: A **527**, 2790 (2010).
24. H. Yu, H. Yu, G. Min, S. S. Park, B. S. You, and Y. M. Kim, Metals and Materials International **19**, 651 (2013).
25. M. Nienaber, G. Kurz, D. Letzig, K. U. Kainer, and J. Bohlen, Crystals **12**, 1307 (2022).

26. I. Dillamore, P. Hadden, and D. Stratford, in (Hindawi, 1970).
27. Y. Li, P. Hou, Z. Wu, Z. Feng, Y. Ren, and H. Choo, Materials & Design **202**, 109562 (2021).